Total variation based gradient descent algorithm for sparse-view photoacoustic image reconstruction

Yan Zhang, Yuanyuan Wang *, Chen Zhang

Department of Electronics Engineering, Fudan University, Shanghai 200437, China

ARTICLE INFO

ABSTRACT

In photoacoustic imaging (PAI), reconstruction from sparse-view sampling data is a remaining challenge in the cases of fast or real-time imaging. In this paper, we present our study on a total variation based gradient descent (TV-GD) algorithm for sparse-view PAI reconstruction. This algorithm involves the total variation (TV) method in compressed sensing (CS) theory. The objective function of the algorithm is modified by adding the TV value of the reconstructed image. With this modification, the reconstructed image could be closer to the real optical energy distribution map. Additionally in the proposed algorithm, the photoacoustic data is processed and the image is updated individually at each detection point. In this way, the calculation with large matrix can be avoided and a more frequent image update can be obtained. Through the numerical simulations, the proposed algorithm is verified and compared with other reconstruction algorithms which have been widely used in PAI. The peak signal-to-noise ratio (PSNR) of the image reconstructed by this algorithm is higher than those by the other algorithms. Additionally, the convergence of the algorithm, the robustness to noise and the tunable parameter are further discussed. The TV-based algorithm is also implemented in the *in vitro* experiment. The better performance of the proposed method is revealed in the experiments results. From the results, it is seen that the TV-GD algorithm may be a practical and efficient algorithm for sparse-view PAI reconstruction.

© 2012 Elsevier B.V. All rights reserved.

1. Introduction

Photoacoustic imaging (PAI) [1–3] is a novel and fast-developing biomedical imaging technique. Due to its noninvasive nature, it attracts extensive attentions and becomes a promising imaging modality. PAI combines the high contrast from the pure optics imaging and the deep penetration from the ultrasound imaging [2]. It is capable of reconstructing the absorbed optical energy distribution image of the biological tissue, which may be useful in many medical applications such as early cancer detection [4,5], vascular imaging [6,7], brain imaging [8] and ocular imaging [9].

PAI is based on the photoacoustic effect [1,2], which is essentially a transformation from the optical energy to the acoustic energy. In the computed-tomographic PAI concerned in this paper, a short-pulse laser is used to irradiate the biological tissue. The absorbed optical energy will lead to the thermoelastic expansion which induces the ultrasound wave in a wide frequency range. A scanning ultrasound transducer or a transducer array is employed to receive the photoacoustic signals. Afterwards, the laser energy deposition image can be calculated from the sampling data by using a reconstruction algorithm.

The reconstruction algorithm is a critical key point in the PAI, and an accurate and efficient algorithm is significant. A considerable amount of research has been done on the topic of reconstruction algorithms. Exact reconstruction algorithms in the time-domain and the frequency-domain have been developed in various scanning geometries [10–13]. Xu et al. proposed the filtered back-projection (FBP) algorithm for the photoacoustic image reconstruction [14,15], which has been widely used for its convenience and accuracy. Zhang et al. proposed the deconvolution reconstruction (DR) method, which has an efficient calculation and a satisfying reconstruction effect in the situation of limited-view sampling angle and heterogeneous acoustic medium [16,17]. Besides, the iterative reconstruction (IR) algorithm has been developed for PAI and it has an improvement of the image quality [18]. Several other reconstruction algorithms were proposed for the PAI using a linear array of transducers [19,20]. However, these methods cannot keep effective when the sampling points are insufficient. In such conditions, the reconstructed images usually become blurred and distorted, and the reconstruction qualities decline severely. For example, when the sampling points are not sufficient, the image reconstructed by the FBP algorithm will be seriously affected by the remaining artifacts, which limits the medical application of PAI.

To reconstruct an image from limited sampling data is still a remaining challenge for PAI in the cases of fast or real-time

---

* Corresponding author.
  E-mail address: yywang@fudan.edu.cn (Y. Wang).

imaging [21]. However, this is a typical ill-posed inverse problem in mathematics. Usually, two main kinds of methods are used to solve the reconstruction problem [22]. Ones estimate the missing data from the received data, and then accomplish the reconstruction with former mentioned algorithms. Here the data interpolation approximation is important, and the redundancy should be noticed. The others reconstruct the images by implementing the iteration, during which the reconstructed image is repeatedly corrected. At the cost of much more calculation time, they have a remarkable compensation for the insufficient photoacoustic dataset. In this way, the quality of the reconstructed image is enhanced significantly.

Recently, Candes and Tao et al. established the compressed sensing (CS) theory [23], which is fast-developing and has been widely applied to many scientific fields including PAI image reconstruction [24,25]. The total variation (TV) method is involved in the CS theory, and it is reported that images can be accurately recovered from sparse data by the TV minimization [26]. The pioneer work of the TV method focuses on the image restoration with the noise removal [27]. Recently, the TV method is extended to the modern biomedical image reconstruction. The algebraic reconstruction technique (ART)-TV [28–30] is proposed for the divergent-beam computed tomography. In the field of PAI reconstruction, the total variation minimization (TVM) is proposed with the TV coefficient involved in the finite element method (FEM) [31]. Besides, the adaptive steepest-descent-projection onto convex sets (ASD-POCS) is proposed [32] with the TV utilized in the iteration.

In this paper, a TV-based gradient descent algorithm (TV-GD) is proposed for sparse-view PAI image reconstruction. The proposed algorithm is based on TV as well as TVM and ASD-POCS. However, there exist major differences between our algorithm and TVM. The TVM method is based on the finite element method (FEM), while we set an objective function to be minimized and implement an iteration to reconstruct the image. Besides, the TVM method accomplishes the reconstruction in the frequency domain, while our reconstruction goes in the time domain. As for the ASD-POCS algorithm, the processes of reconstructing the image and enforcing the TV constraint are separated, while in our algorithm, the TV constraint is calculated along with the reconstruction, which is realized by modifying the objective function. Additionally, in our algorithm, the measurement matrices are calculated and the data is processed individually at each detection point, so that the reconstructed image is updated after the iteration at each detection point. Such a different update procedure is useful to avoid the excess calculation of large-sized matrices and the reconstructed image can be updated more frequently. As a result, it is expected that the TV-GD algorithm could be faster than the ASD-POCS algorithm.

Through the numerical simulation, the TV gradient descent reconstruction algorithm is verified and compared with several other algorithms, including the FBP, the DR and the IR methods. The reconstructions of these algorithms are analyzed qualitatively and quantitatively. The calculation speed of this algorithm is also compared with other CS-based algorithm. Besides, the convergence of the TV-GD algorithm and the robustness to noise are discussed. The theory of the algorithm is described in Section 2. The simulation is introduced in Section 3. The performance of the TV-GD algorithm is demonstrated by the *in vitro* experiments with our PAI system, as presented in Section 4. Section 5 is the conclusion.

2. Theory and method

2.1. Photoacoustic theory

In this paper, the two-dimension PAI is studied in our numerical simulations and experiments. For a spatially uniform laser illumination, the relationship between the photoacoustic signals and the laser energy deposition can be derived as the following wave equation [33]

$$\nabla^2 p(\mathbf{r}, t) - \frac{1}{c^2} \frac{\partial^2 p(\mathbf{r}, t)}{\partial t^2} = -\frac{\beta}{C_p} A(\mathbf{r}) \frac{\partial I(t)}{\partial t}, \tag{1}$$

where $p(\mathbf{r}, t)$ is the acoustic pressure at the position $\mathbf{r}$ and the time t, c is the sound speed in the tissue, β is the isobaric expansion coefficient, C_p is the specific heat, $A(\mathbf{r})$ is the spatial deposition of the absorbed laser energy and $I(t)$ is the temporal profile of the laser pulse.

By using the Green's function, Eq. (1) can be solved and the detected acoustic pressure can be expressed as [33]:

$$p(\mathbf{r}_0, t) = \frac{\beta}{4\pi C_p} \frac{\partial}{\partial t} \oiint_{|\mathbf{r}' - \mathbf{r}_0| = ct} \frac{A(\mathbf{r}')}{t} d^2 \mathbf{r}', \tag{2}$$

where $\mathbf{r}_0$ is the position of the transducer.

The photoacoustic signals at different positions can be obtained by moving the transducer. After collecting a set of photoacoustic data, the image can be reconstructed from the measured signals. This image reconstruction is regarded as an inverse problem, and the exact reconstruction equation has been deduced [10] as follows:

$$A(\mathbf{r}) = -\frac{C_p r_0^2}{2\pi \beta c^4} \int \int_{S_0} \frac{1}{t} \frac{\partial p(\mathbf{r}_0, t)}{\partial t} \bigg|_{|\mathbf{r}' - \mathbf{r}_0| = ct} dS_0, \tag{3}$$

where $\mathbf{r}_0$ is the norm of the vector $\mathbf{r}_0$, meaning the radius of the scanning circle.

Another way to solve the reconstruction problem is iteration. The relationship between the detected signals and the absorbed optical energy deposition can be represented as a matrix multiplication. We can calculate the photoacoustic signals based on the reconstructed image, so the iterative reconstruction algorithm repeatedly corrects the reconstructed image to make the calculated signals close to the real signals. The iteration is terminated if the error of the signals is below a preset level, then the reconstructed image can be obtained.

When the sampling views are sparse and the total number of the detection points is insufficient, the reconstructed image is often degraded by artifacts. Therefore, we aim to solve the insufficient data problem as discussed in the following paragraph.

2.2. Total variation theory

The CS theory is an innovative information theory. It has been fully-developed and further-extended into many aspects of scientific researches. According to the CS theory, the signal is sparse in a certain domain (e.g. the Fourier domain or the wavelet domain). By minimizing the l_1-norm in that domain, the signal can be exactly recovered from the relatively less knowledge [26]. As for an image, the grayscale value is not sparse in general, but the discrete gradient matrix is supposed to be sparse. Labeling the grayscale value of the image as $f_{i,j}$, the magnitude of the discrete gradient can be calculated as

$$grad(f_{i,j}) = \sqrt{(f_{i,j} - f_{i-1,j})^2 + (f_{i,j} - f_{i,j-1})^2}. \tag{4}$$

Taking the Shepp–Logan image in Fig. 1a for example, the size of the image is 128 pixels × 128 pixels. The number of non-zero pixels in the original image is 8040, while in the discrete gradient matrix as shown in Fig. 1b, the number of non-zero elements is 747. The sparseness of the discrete gradient matrix is evident by comparison.

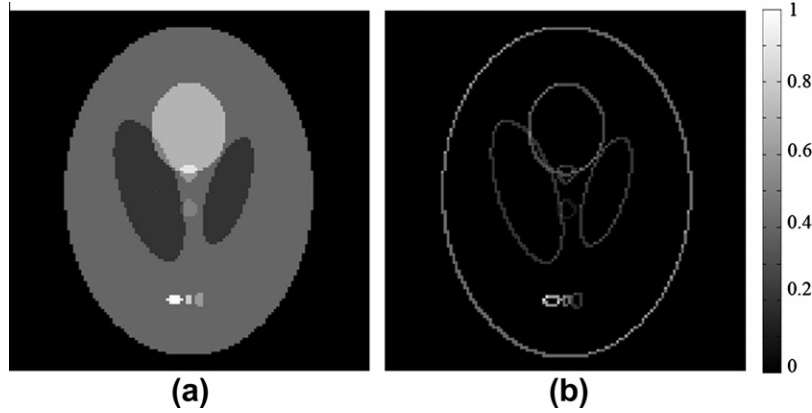The total variation value is the l_1-norm of the discrete gradient matrix,

Fig. 1. (a) The Shepp–Logan image and (b) magnitude of discrete gradient matrix of the Shepp–Logan image.

$$TV(f) = \sum_{i,j} \sqrt{(f_{i,j} - f_{i-1,j})^2 + (f_{i,j} - f_{i,j-1})^2}. \tag{5}$$

where (i,j) is the coordinate of the image f.

It is reported in the literature [26] that the image can be accurately recovered from the sparse sampling data in Fourier domain by minimizing the TV value. Here, we will introduce the TV method and investigate a new algorithm for the sparse-view PAI image reconstruction.

2.3. TV-based PAI reconstruction algorithm

In this part, we provide the procedures of the TV-based PAI reconstruction algorithm.

For a succinct expression, we define a new variable g as

$$g(\mathbf{r}_0, t) = \frac{4\pi C_p t}{\beta} \cdot \int_0^t p(\mathbf{r}_0, t)dt. \tag{6}$$

Integrating both sides of Eq. (6) and substituting g into the equation lead to

$$g(\mathbf{r}_0, t) = \oiint_{|\mathbf{r}_0 - \mathbf{r}'| = ct} A(\mathbf{r}')d\mathbf{r}'. \tag{7}$$

Notice that the signal g at the position $\mathbf{r}_0$ is a linear integration of the $A(\mathbf{r})$ along an arc whose center is $\mathbf{r}_0$ and radius is ct.

In the proposed reconstruction algorithm, the reconstructed image and the measured signals are processed discretely. The photoacoustic image $\mathbf{A}$ is discretized into a grid of N_x pixels $\times N_y$ pixels, and then $\mathbf{A}$ is reshaped into a vector $\mathbf{A}'$ with a size of $N_x N_y$ rows $\times 1$ column. Supposing that the size of measured vector g is T rows $\times 1$ column, we can define a measurement matrix $\mathbf{W}$ [18], converting the Eq. (7) into matrix multiplication form:

$$g(i) = \mathbf{W}(i) \cdot \mathbf{A}', \quad i = 1, 2, 3, \ldots, M. \tag{8}$$

where $\mathbf{W}$ is with a size of T rows $\times N_x N_y$ columns and M is the total number of the detection points.

At each sampling point, the local measurement matrix $\mathbf{W}$ can be calculated as

$$\mathbf{W}_{jk}(i) = \begin{cases} 1 - \left| \frac{t_j}{\Delta t} - \frac{|\mathbf{r}_k - \mathbf{r}_i|}{c\Delta t} \right| & \text{when } \left| \frac{t_j}{\Delta t} - \frac{|\mathbf{r}_k - \mathbf{r}_i|}{c\Delta t} \right| < 1 \\ 0 & \text{else} \end{cases}, \quad i = 1, 2, 3, \ldots, M. \tag{9}$$

where c is the sound speed, Δt is the discretized time step, t_j is the jth temporal measurement at the ith detection point, $\mathbf{r}_k$ is the position of the kth point in the reconstructed image, $\mathbf{r}_i$ is the position of the ith detection point, and M is the total number of the detection points.

In the proposed algorithm, the data is processed separately at each detection point. Otherwise the $\mathbf{W}$ matrix will be extremely large. For instance, assuming that the size of the reconstructed image is 128 pixels $\times$ 128 pixels, the length of the discretized signal $T = 120$ and the total number of the detection points $M = 90$, the total number of elements in $\mathbf{W}$ is nearly 1.77×10^8. It is impractical to calculate the inverse matrix or pseudo-inverse matrix to accomplish the reconstruction. If the large matrix $\mathbf{W}$ is used for the iteration, the repeatedly calculation with $\mathbf{W}$ wastes a lot of time. While in our algorithm, the data is separately processed at each detection point, so that the measurement matrix $\mathbf{W}$ is much smaller and the calculation at each iteration step reduces significantly. Though more times of iterations are needed, it is still expected to be more calculation efficient. Additionally, such a frequent update is good to get a better convergence.

Eq. (8) shows the relationship between the received signals and the absorbed energy deposition. In the proposed algorithm, the TV parameter is involved into the iteration. Different from the IR algorithms, under the constraint given by (8), we aim to obtain the reconstructed image with the smallest TV value. It can be expressed mathematically as

$$\min TV(\mathbf{A}) \quad s.t. \quad g = \mathbf{W}(i) \cdot \mathbf{A}', i = 1, 2, 3, \ldots, M. \tag{10}$$

This is a typical form in the CS reconstruction. The reconstruction can be converted into an optimization problem:

$$\min_A \{\|\mathbf{W} \cdot \mathbf{A}' - g\|_2^2 + a \cdot TV(\mathbf{A})\}. \tag{11}$$

The first term in the objective function relates to Eq. (8) and the second term assures an image solution with a small TV value. Note that, if the second term becomes dominate in the objective function, the data fidelity will be affected and sacrificed to the image regularity. Thus, we set a tunable parameter a for balancing these two parts of the objective function. These two parts respectively denote the data fidelity and the image regularity. If an appropriate parameter is employed, both the data fidelity and the image regularity can be maintained, and the selection of the optimal a value will be discussed in the following section.

The gradient descend method is utilized to decrease the objective function in order to accomplish the reconstruction

$$\Delta \mathbf{A} = -\frac{\mathbf{W}(i)}{\|\mathbf{W}(i)\|}(\mathbf{W}(i) \cdot \mathbf{A}' - g(i)) - a \cdot \frac{\partial TV(\mathbf{A})}{\partial \mathbf{A}}. \tag{12}$$

During this step, the derivative of the TV with respect to the matrix $\mathbf{A}$ is needed, and this derivative matrix is also reshaped into a column vector for convenience of calculation. Based on the Eq. (5), the derivative can be calculated.

$$\frac{\partial TV(\mathbf{A})}{\partial \mathbf{A}}\Big|_{i,j} = \frac{\partial \sum_{i,j}\sqrt{(\mathbf{A}_{i,j}-\mathbf{A}_{i-1,j})^2+(\mathbf{A}_{i,j}-\mathbf{A}_{i,j-1})^2}}{\partial \mathbf{A}_{i,j}}$$

$$= \frac{\partial\sqrt{(\mathbf{A}_{i,j}-\mathbf{A}_{i-1,j})^2+(\mathbf{A}_{i,j}-\mathbf{A}_{i,j-1})^2}}{\partial \mathbf{A}_{i,j}}$$

$$+ \frac{\partial\sqrt{(\mathbf{A}_{i+1,j}-\mathbf{A}_{i,j})^2+(\mathbf{A}_{i+1,j}-\mathbf{A}_{i+1,j-1})^2}}{\partial \mathbf{A}_{i,j}}$$

$$+ \frac{\partial\sqrt{(\mathbf{A}_{i,j+1}-\mathbf{A}_{i,j})^2+(\mathbf{A}_{i,j+1}-\mathbf{A}_{i+1,j})^2}}{\partial \mathbf{A}_{i,j}}$$

$$= \frac{2\cdot\mathbf{A}_{i,j}-\mathbf{A}_{i-1,j}-\mathbf{A}_{i,j-1}}{\sqrt{(\mathbf{A}_{i,j}-\mathbf{A}_{i-1,j})^2+(\mathbf{A}_{i,j}-\mathbf{A}_{i,j-1})^2}+\varepsilon}$$

$$- \frac{\mathbf{A}_{i+1,j}-\mathbf{A}_{i,j}}{\sqrt{(\mathbf{A}_{i+1,j}-\mathbf{A}_{i,j})^2+(\mathbf{A}_{i+1,j}-\mathbf{A}_{i+1,j-1})^2}+\varepsilon}$$

$$- \frac{\mathbf{A}_{i,j+1}-\mathbf{A}_{i,j}}{\sqrt{(\mathbf{A}_{i,j+1}-\mathbf{A}_{i,j})^2+(\mathbf{A}_{i,j+1}-\mathbf{A}_{i-1,j+1})^2}+\varepsilon}, \tag{13}$$

where $\frac{\partial TV(\mathbf{A})}{\partial \mathbf{A}}\big|_{i,j}$ is the element located in the ith row and the jth column of the derivative matrix, and ε is a small positive number used to avoid a zero denominator, assigned 10^{-8} in practice.

According to Eq. (12), the matrix $\mathbf{A}$ is updated M times at each sampling point. Then the iteration is repeated unless the existing condition is met. Generally the exiting criterion is set as that the error is under a certain level or the iteration number is more than a pre-specified number.

Finally in this section, the TV-GD algorithm is summarized in three steps as follows:

(1) Initialization: Apply Eq. (6) to get g after the discretization. Then apply Eq. (9) to calculate the measurement matrixes $\mathbf{W}(i)$, and the reconstructed image is initialized to be zero matrix.

(2) Iteration: For $i = 1, 2, 3, \ldots, M$, implement the iteration as

$$\Delta\mathbf{A} = -\frac{\mathbf{W}_i}{\|\mathbf{W}_i\|}(\mathbf{W}_i\cdot\mathbf{A}'-g(i))-a\cdot\frac{\partial TV(\mathbf{A})}{\partial\mathbf{A}}. \tag{14}$$

(3) Update or termination: When the exiting criterion (e.g. the error threshold or the iteration number) is met, end the iterations, otherwise update the image matrix $\mathbf{A}$ and return to step (2).

3. Numerical simulations

To validate the proposed TV-based gradient descent reconstruction algorithm, the simulation experiments are performed using Matlab (version 7.8.0.0347) on a PC with 2.0 GHz Quad-CPU and 2.93 GB memory. The original absorbed laser energy distribution map is set as the Shepp–Logan image shown in Fig. 1a, which is often used in the evaluation of tomographic reconstruction algorithms. The sound speed is 1500 m/s, which is consistent in the simulation.

The quality of the reconstructed image, the convergence, the robustness of the algorithm, and the tunable parameter a are going to be discussed as follows.

3.1. Sparse-view reconstruction

In the simulation, the size of the simulation area is 102.4 mm × 102.4 mm, and the radius of the scanning circle is 48 mm. In order to compare the performance of the TV-GD algorithm with different amount of sampling views, four different situations are simulated. In these four cases, the sampling angles cover 360° around the imaging object, the angular step size is uniform and set to 2.25°, 4°, 6° and 12°, respectively. Then by Eq. (2), we can calculate the photoacoustic signals in the condition that the number of the sampling points is 160, 90, 60 and 30. These simulated signals are termed as 160-view, 90-view, 60-view and 30-view data correspondingly. Based on these simulated photoacoustic data, the image reconstruction is carried out. Besides the TV-GD algorithm, the FBP, the DR the IR and the ASD-POCS algorithms are utilized for comparison.

It is necessary to point out that the numbers of iteration times are all set to 10, we do not set the error threshold as the iteration criterion, because we want to compare the iterative algorithms after the same iteration numbers. The tunable parameter a in TV-GD algorithm is set to 0.2. The sizes of the reconstructed images are 128 pixels × 128 pixels. The simulation results by using these different methods are shown in Fig. 2.

It is shown in the first column of Fig. 2 that the FBP, the IR, the ASD-POCS and the TV-GD have comparable reconstruction qualities in the condition of sufficient sampling data. Only for the DR, the reconstructed image as shown in Fig. 2e becomes blurred and the small ellipses are difficult to recognize.

When the number of sampling points decreases, the qualities of the reconstructions are affected in the FBP, DR and IR reconstructions. For the FBP reconstruction, because the sampling views become sparser, more back-projection arcs cannot be canceled out with each other. These arcs would remain conspicuous in the reconstructed image, leading to the degradation of the image quality. The DR images are more ambiguous and the edge information is not effectively preserved. The IR images are easier to be affected by the noise, and its signal-to-noise ratio (SNR) decline. Comparatively, the ASD-POCS and the TV-GD images have been remaining in a high quality level and visually indistinguishable as the number of sampling points decreases. It is revealed that the TV-GD algorithm can provide an equivalent reconstruction as the ASD-POCS reconstruction.

In the extremely sparse sampling condition with 30 angles (smaller than those used in [14,16]), the TV-GD reconstruction is still accurate while the images reconstructed by the FBP, the DR and the IR algorithms are severely distorted. In the IR reconstructed image, the noise is not effectively depressed. In the ASD-POCS and the TV-GD image, the image noise is depressed better than the above three algorithms. It is shown in the comparison in the bottom row of Fig. 2 that the number of sampling points does not substantially affect the quality of the TV-GD reconstruction.

In order to provide numeric quantification of the results, the peak signal-to-noise rations (PSNRs) of the reconstructed images are adopted with the phantom image as standard.

$$PSNR = 10\cdot\log_{10}\left(\frac{N_x N_y}{\sum_{i=1}^{Nx}\sum_{j=1}^{Ny}(f_{i,j}-r_{i,j})^2}\right). \tag{15}$$

where f is the gray-value of the reconstructed image and r is the gray-value of the phantom. The size of the image is $N_x \times N_y$.

We calculate the PSNRs of the reconstructed images for four different simulation conditions by using different reconstruction algorithms. The quantitative results are shown in Table 1.

It is shown in Table 1 that the quantitative results correspond with the visual comparisons. For the FBP algorithm, due to the minus pixels in the reconstructed images, the PSNRs keep in an extremely low level. In the sparse-view sampling conditions, the PSNRs of the images reconstructed by the TV-GD algorithm are the highest. It can be derived that the TV-GD algorithm is more accurate than other algorithms in the sparse-view sampling condition.
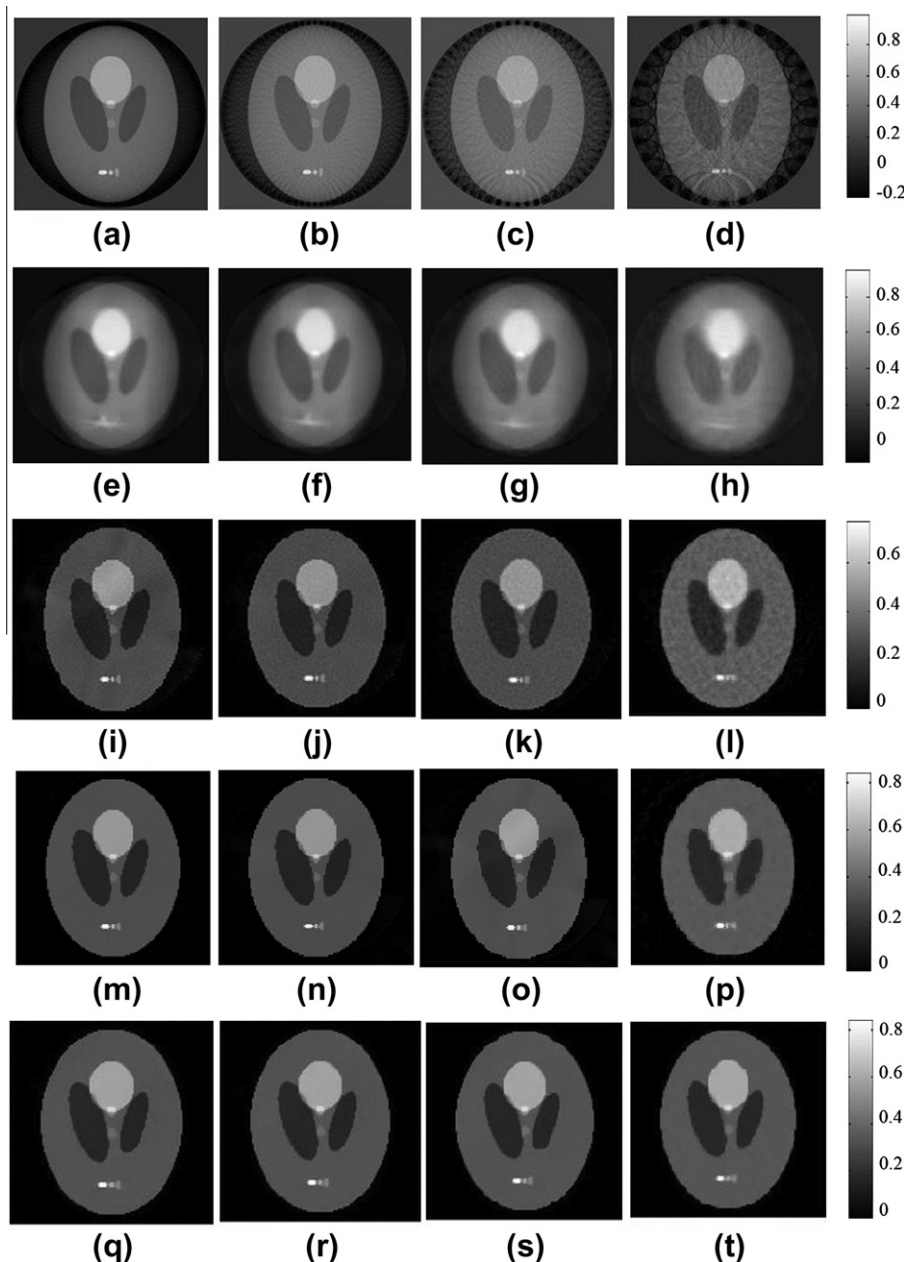
Fig. 2. The first to fifth rows refer to the FBP, DR, IR, ASD-POCS and TV-GD reconstructed images respectively and the first to fourth columns refer to the results from 160-view, 90-view data, 60-view and 30-view data respectively.

We continuously decrease the number of the detect points in order to investigate the lower limit of the sampling points. As we set the criterion of acceptability that the PSNR of the reconstructed image reaches 30 dB. It is found out that the total number of the sampling points is able to be reduced to 18 for TV-GD algorithm.

In order to show the detail qualities of reconstructed images clearly, we draw a row of pixels (shown in Fig. 3a by dotted line) from each image reconstructed from 30-view data. The comparisons of pixel profiles are displayed in Fig. 3b and c.

In Fig. 3b, the solid line, the dotted line and the dash dotted line represent the pixel profiles of the original image, FBP image and DR image, respectively. In Fig. 3c, the solid line, the dotted line, the dash line and the dash dotted line represent the pixel profiles of the original image, IR image, the ASD-POCS and TV-GD image, respectively.

Table 1
PSNRs (dB) of reconstructed images.

	160-view	90-view	60-view	30-view
FBP	15.35	15.36	15.24	14.68
DR	21.63	21.45	21.29	21.19
IR	33.83	34.98	34.21	31.19
ASD-POCS	35.17	35.05	34.71	33.72
TV-GD	38.01	38.23	38.18	36.68

It is shown in Fig. 3b that the profiles of the FBP image and the DR image significantly differ from the original profile. Because of the severe artifacts in the FBP image, there exist huge vibrations in the profile. While in Fig. 3c, the profile of the ASD-POCS, TV-GD image and the original profile match precisely. In order to compare

them clearly, we calculate the quadratic sum of the reconstruction error and make a comparison. The quadratic sums are 0.0632, 0.0673 and 0.1335 respectively for the TV-GD, the ASD-POCS and the IR algorithms, and the sums by FBP and DR algorithms are much larger, 1.6531 and 1.0674, respectively. This comparison denotes that the TV-GD reconstructed image is the closest to the original image.

From the above discussions, the TV-GD algorithm is proved to be an accurate and stable algorithm in sparse-view photoacousitc image reconstruction.
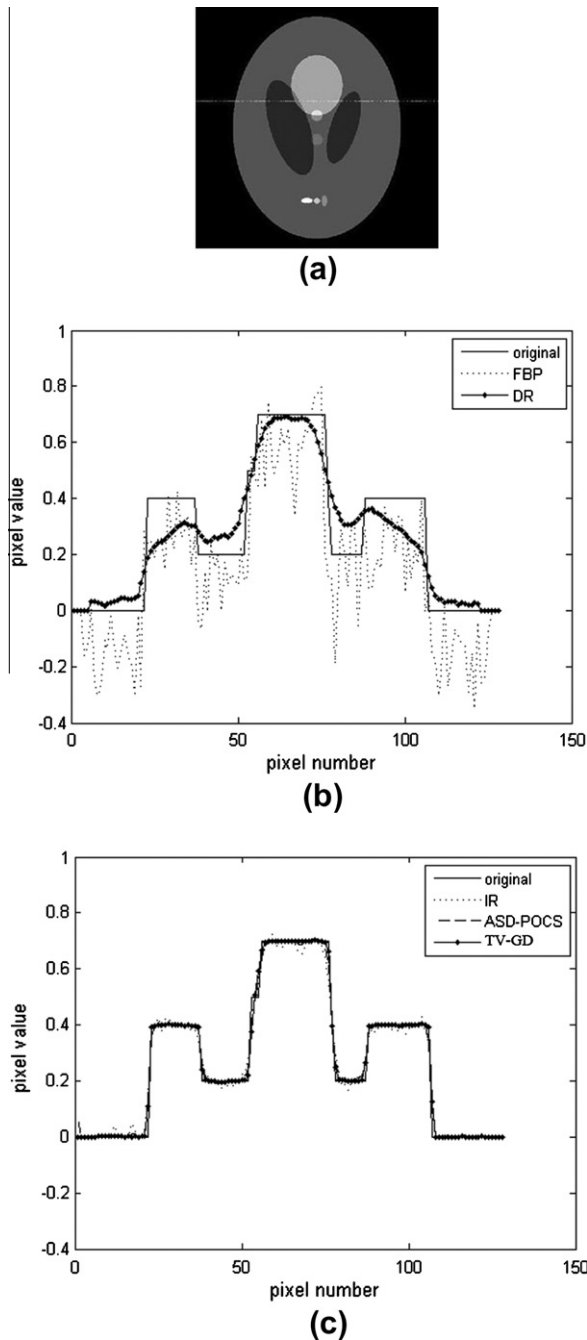
3.2. Convergence and calculation

To further study the convergence of the TV-GD algorithm, a distance between the reconstructed image and the phantom image is defined as

$$d = \left(\frac{\sum_{i=1}^{Nx}\sum_{j=1}^{Ny}(f_{i,j} - r_{i,j})^2}{\sum_{i=1}^{Nx}\sum_{j=1}^{Ny} r_{i,j}^2} \right)^{1/2}. \tag{16}$$

where f is the reconstructed image and r is the phantom. The size of the image is $N_x \times N_y$. This distance d with a smaller value denotes that the reconstructed image is closer to the original phantom image and vise versa.
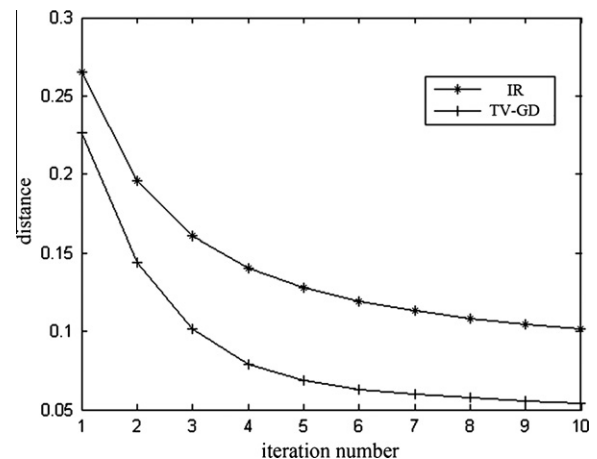
Since the different update procedures in the ASD-POCS and the TV-GD algorithms, we select IR algorithm to have a comparison with TV-GD algorithm on the convergence. We computed the previously defined distance of both IR and TV-GD algorithms after each iteration step, and the distance values versus the iteration number are depicted in Fig. 4, in which the line '*−' refers to the traditional IR algorithm and the line '+−' refers to the TV-GD algorithm.

It is revealed in Fig. 4 that the reconstructed image by the TV-GD has a smaller distance to the phantom image and the distance reduces more quickly than the IR algorithm. It can be inferred that the TV-GD reconstruction is more accurate and the convergence of the TV-GD is faster.

Since we have modified the objective function of the iteration, and the gradient descent method is added in the reconstruction to decrease the TV of the image, additional calculation is necessary compared to the IR algorithm. However, in the simulation experiments, we find that the time cost in the TV procedure occupy a tiny part in the entire time cost in the algorithm. In other words, the adoption of TV calculation will not lead to a great increase of the calculation time. Take the simulation demonstrated in Section 3 a for example. The number of sampling points is 30 and the length of the discretized signal is 120. To reconstruct an image in a size of 128 pixels × 128 pixels with 10 iteration steps, it takes 25.30 s by using the IR algorithm and 25.98 s by using the TV-GD algorithm. The extra calculation time is ignorable.

As for the ASD-POCS, another TV based algorithm, the it has to repeatedly calculate with the large measurement matrix, and the update procedure costs more time than the TV-GD method. In the same numerical simulation, it takes 484.84 s to accomplish the reconstruction, much more than the TV-GD method.

The algorithm reported in [24] is also based on compressed sensing, and it is much more computationally intensive. It takes

Fig. 3. (a) The location of the pixel profile in the image. (b), (c) The gray-scale profiles of the original image and the reconstructed images from 30-view data by the FBP, DR, IR, ASD-POCS and TV-GD algorithms respectively.

Fig. 4. The distance between the reconstructed images and the original phantom image versus the iteration number.

10–15 h [24] to reconstruct an image in a size of 256 pixels × 256 pixels. To reconstruct an image in a same size, the TV-GD method takes only 213 s.

From the above discussion, it could be concluded that the TV-GD algorithm is more efficient in calculation.

3.3. Robustness to noise

In this part, we will analyze the noise robustness of the TV-GD algorithm. In the progress of the signal acquisition, the detected photoacoustic signals are usually affected by thermal noises from the ultrasound transducer and the system electronics, and these are white Gaussian noises. So here, the 30-view simulated signals are added with white Gaussian noises of different powers. Based on these noisy signals, the images can be reconstructed. The reconstructed images by the IR and TV-GD algorithms are shown in Fig. 5, where the SNR of the simulated noisy signals is 10 dB, 5 dB, 3 dB and 0 dB, respectively.

The TV-GD reconstructed image from the signals with an SNR of 10 dB, as shown in Fig. 5b, has hardly any difference with the image reconstructed from noise-free signals shown in Fig. 2t. The TV-GD image quality is superior to the IR algorithm with better noise robustness.

With stronger noise, the quality of reconstruction declines. When the SNR deteriorates to 0 dB, there is no longer a visible advantage of the TV-GD algorithm comparing to the IR algorithm. In this case, the noise suppression is worth of further studies.

3.4. Adaptive tunable parameter investigation

As mentioned before, this algorithm contains a tunable parameter a as given in Eq. (12), which is used for balancing two parts of the objective function. Here we present a further investigation of this tunable parameter and the selection of the optimal a parameter.

This parameter with a big value denotes that the TV constraint is dominating, and it is expected that the reconstruction would have a quicker convergence. However, a too big value will break the balance between two parts of the objective function, and the data fidelity will be affected. The reconstructed image may have a comparative small TV, but the image is quite different from the real photoacoustic image, because the data fidelity in the reconstruction is sacrificed to image regularity. The quality of the reconstruction declines very much.

In this case, an adaptive parameter is supposed to provide a solution. The parameter a is set to a comparable bigger value to obtain a quicker convergence at the beginning. As the iteration goes, a becomes smaller so that the data fidelity will be emphasized and the final reconstructed image can be closer to the real image.

The adaptive parameter a is defined as

$$a = \begin{cases} 2/n & 1 \leq n \leq 10 \\ 0.2 & n \geq 11 \end{cases}, \tag{17}$$

where n is the iteration number.

We test this parameter with several different constant values and the adaptive parameter, and the reconstructed images are shown in Fig. 6.

It is found in Fig. 6d that when the a is too big, the reconstructed image will be over smoothed and the spatial resolution of the reconstructed image will be very low. When the value of a parameter is selected in a proper range ($0.2 < a < 1$), the reconstructed images are visually similar and the spatial resolution are not affected. Otherwise, this parameter will make an influence to the convergence of the reconstruction, we record the distances defined in Eq. (16) between the reconstructed image and the original phan-
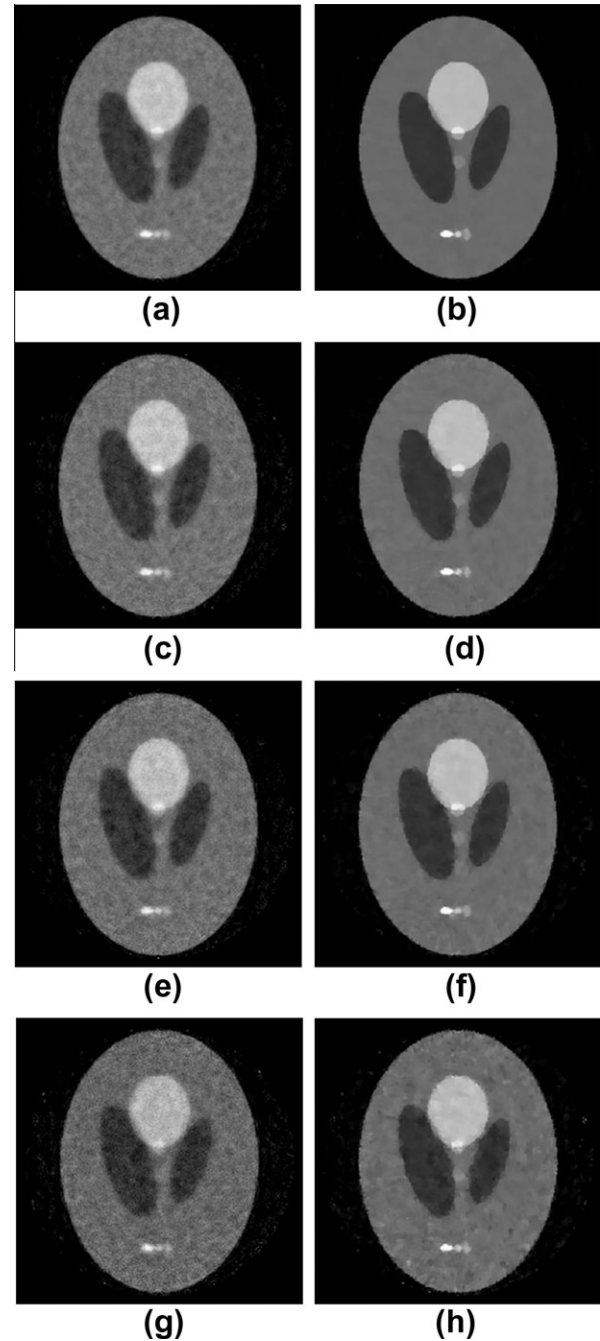

Fig. 5. Left and right columns show images reconstructed by the IR and TV-GD algorithm, respectively, from signals with SNR of (a, b) 10 dB, (c, d) 5 dB, (e, f) 3 dB and (g, h) 0 dB.
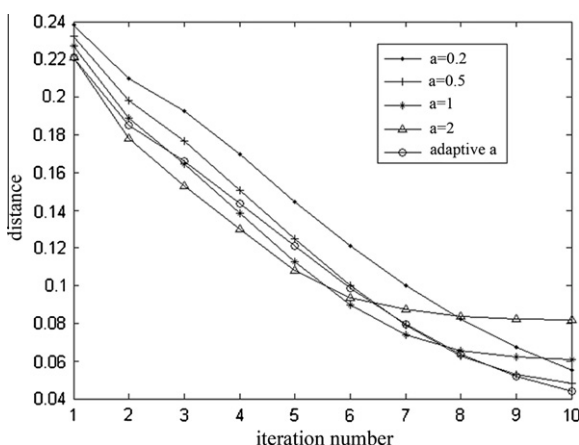
tom image after each iteration step. The curves of distances in the TV-GD reconstructions with the different a parameter are depicted in Fig. 7.

In Fig. 7, the lines '·−', '+−', '*−' and '△−' represent the curves of distance when the parameter a is set to 0.2, 0.5, 1 and 2 respectively, the line 'o−' represents the curve with adaptive a.

The simulation result is as expected. After several beginning iterations, the a with a big value helps to get a fast convergence, and the value of a decreases as the iteration goes. While the reconstruction accomplishes, the a is small and the image will not be over smoothed, and the spatial resolution will not be impacted. It is also revealed in Fig. 7 that after 10 iteration steps, the distance
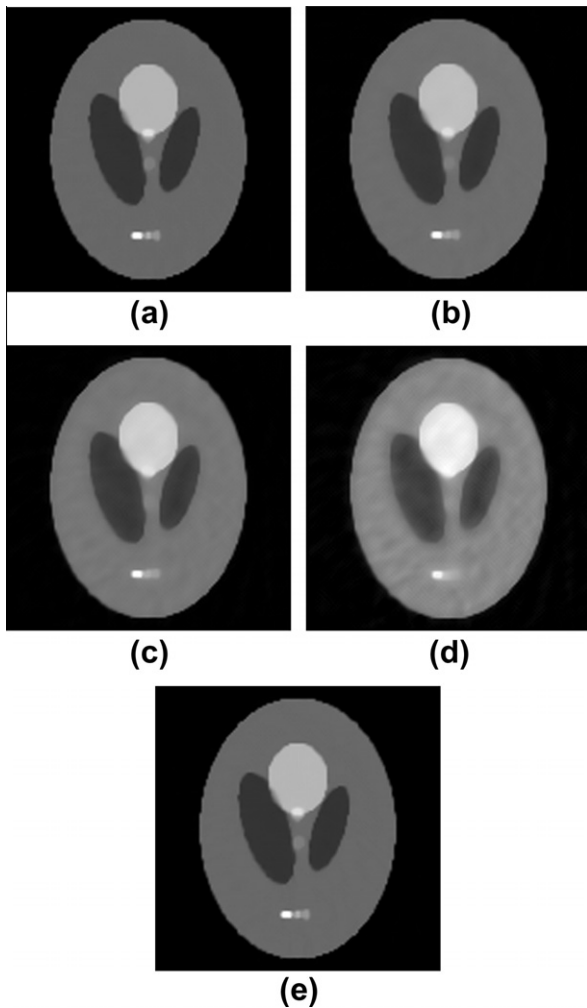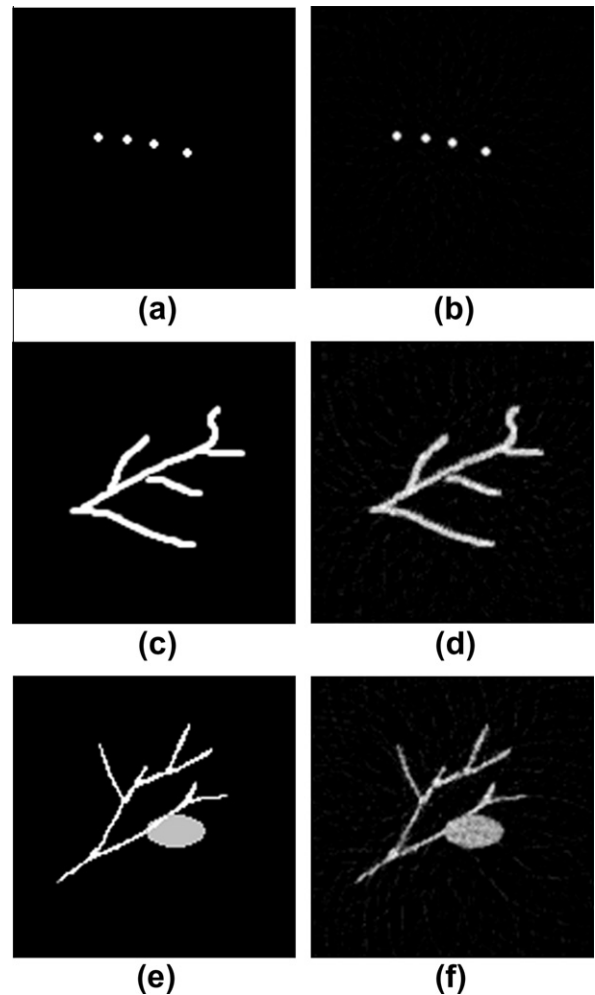
Fig. 6. The TV-GD reconstructed images with different *a* parameters. (a) *a* = 0.2, (b) *a* = 0.5, (c) *a* = 1, (d) *a* = 2, (e) adaptive *a*.

Fig. 8. The TV-GD reconstructed images with different imaging objectives. The left column (a), (c), (e) show the given images, and the right column (b), (d), (f) show the reconstructed images.

Fig. 7. The distance between the reconstructed image and the phantom versus the iteration number with the parameter *a* of different values.

between the reconstructed image and the phantom image with the adaptive *a* is the smallest.

As for the universality of the adaptive parameter and the TV-GD method, we select three different image as the given optical energy deposition to test the universality. The image objects in these three

images are different, which respectively stand for the tiny strong optical absorbers, the vessels and the vessels with the soft tissue. By using the adaptive parameter, the TV-GD reconstructed images are shown in Fig. 8.

It can be found in Fig. 8 that the TV-GD algorithm can be used for reconstructing various imaging objects. The TV-GD is a practical reconstruction algorithm for PAI reconstruction. Additionally, the choice of parameter *a* is independent with the imaging object, and the adaptive *a* can provide a qualified reconstruction.

From these simulations, it can be seen that taking into account both the convergence speed and the quality of reconstructed image, the performance of the proposed TV-GD algorithm can be improved by employing the adaptive parameter *a*.

4. *In vitro* experiments

The proposed TV-GD reconstruction algorithm is also verified through the *in vitro* experiments. The experimental system employing a circularly scanning transducer is illustrated in Fig. 9.

In this system, an Nd:YAG laser generator (Continum, Surelite I) is used. The wavelength of the emitting laser is 532 nm, the pulse width is 5–7 ns and the repetition rate is 10 Hz. The laser energy density in the illumination area is about 6.47 mJ cm^{-2}, lower than the ANSI laser radiation safety standard 20 mJ cm^{-2} [2]. A water-immersion ultrasound transducer (Panametric, V383-SU) is used

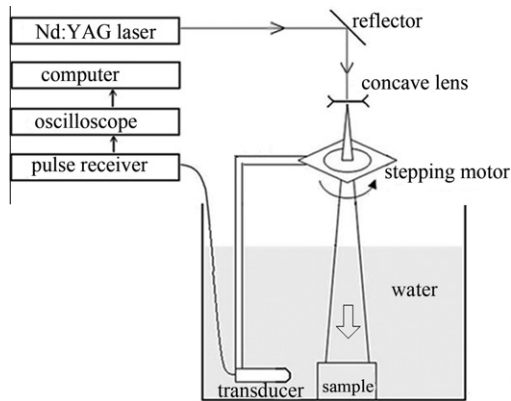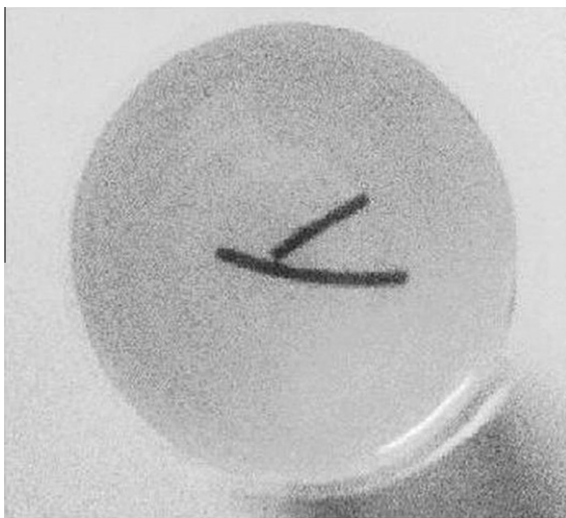**Fig. 9.** The scheme of the PAI experimental system.

Fig. 10. The photograph of the imaging sample.

to receive the photoacoustic signals. The transducer is unfocused and the diameter of the active element is 9.525 mm. The central frequency is 3.5 MHz and the bandwidth is 1.12 MHz. The analog ultrasound signals are amplified by the pulse receiver (Panametric, 5900PR) and sampled into digital signals by the oscilloscope (Agilent, 54622D). The sampling frequency is set to 16.67 MHz. Then the sampled data is transported to the computer through the general purpose interface bus (GPIB). Besides, the position of the transducer is controlled by a digital stepping motor (GCD-0301 M), which is connected to the computer with the universal serial bus (USB).

In this experiment, the imaged sample is a gelatin cylinder with two rubber bars embedded as the optical absorbers. The radius of the gelatin cylinder is 25 mm. The photograph of the sample is shown in Fig. 10.

In the experiment, the scanning radius is 38 mm. For comparison, we sampled two sets of photoacoustic signals when the angular step is 4° and 12°, respectively. So 90-view data and 30-view data are collected for the reconstruction. The images are reconstructed by the FBP, the DR, the IR, the ASD-POCS and the TV-GD algorithms, respectively, which are shown in Fig. 11. Necessary to point out is that the iteration numbers of the iterative algorithms are all set to 10.

We can find out from the left column of Fig. 11 that these algorithms are all effective in the sufficient data condition. Two laser absorbers are clearly shown in the reconstructed images. In the
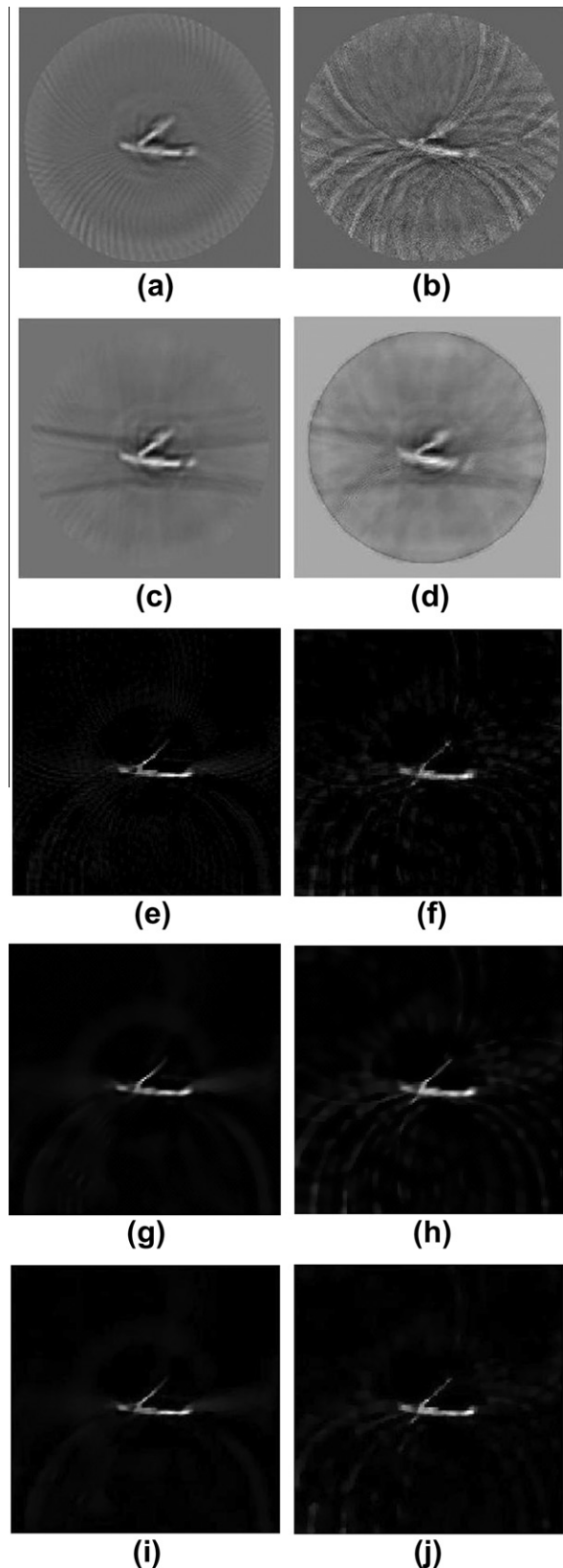

Fig. 11. The reconstructed images from 90-view and 30-view data, respectively, by (a, b) the FBP, (c, d) the DR, (e, f) the IR, (g, h) the ASD-POCS and (i, j) the TV-GD algorithms.

sparse-view sampling condition as shown in the right column, there exist great differences among the five algorithms. The FBP reconstructed image is badly distorted by plenty of artifacts, and

it is difficult to recognize the laser absorbers out of the artifacts. The DR image is blurred and the edges of the absorbers are ambiguous. In the background of the IR image, the noise is not effectively depressed.

By contrast, the three iterative algorithms provide higher-quality images. In the TV-GD image, the two optical absorbers are distinct, similar as the sufficient data condition, the quality is not essentially affected, and the entire image is less affected by the noise.

The better performance of the TV-GD algorithm in sparse-view PAI is revealed through the *in vitro* experiments. It is also shown in Fig. 11i and j that in the sparse-view sampling condition, the TV-GD algorithm can provide a stable and accurate reconstruction.

5. Conclusion

In this paper, the total variation method is successfully applied to the PAI, and the TV-based gradient descent algorithm is proposed for the image reconstruction. Different from the existed iterative algorithm, we utilize the sparseness of the image's discrete gradient matrix and modified the objective function by adding the TV value. In the proposed method, the gradient descent method is used to obtain a reconstructed image with a comparatively smaller TV value. Additionally, we processed the photoacoustic data individually at each detection point to obtain a more frequent image update and a less calculation. This algorithm has been validated by numerical simulations and *in vitro* experiments. The algorithm convergence, the robustness to noise and the tunable parameter are also discussed. Through qualitative and quantitative analysis, the good performance of the TV-GD algorithm is revealed. The reconstruction with TV-GD is stable and the reconstructed images remains in high quality as well as the sufficient data condition. Therefore, it could be concluded that the TV-GD algorithm may be a practical algorithm for the sparse-view PAI reconstruction.

Acknowledgment

References

[1] C. Li, L.V. Wang, Photoacoustic tomography and sensing in biomedicine, Phys. Med. Biol. 54 (19) (2009) R59–R97.
[2] M. Xu, L.V. Wang, Photoacoustic imaging in biomedicine, Rev. Sci. Instrum. 77 (4) (2006). 041101-1-041101-22..
[3] L.V. Wang, Prospects of photoacoustic tomography, Med. Phys. 35 (12) (2008) 5758–5767.
[4] B. Guo, J. Li, H. Zmuda, M. Sheplak, Multyfrequency microwave-induced thermal acoustic imaging for breast cancer detection, IEEE Trans. Ultrason. Ferroelectr. Freq. Control 54 (11) (2007) 2000–2010.
[5] M. Pramanik, G. Ku, C. Li, L.V. Wang, Design and evaluation of a novel breast cancer detection system combining both thermoacoustic (TA) and photoacoustic (PA) tomography, Med. Phys. 35 (6) (2008) 2218–2223.
[6] J.J. Niederhauser, M. Jaeger, R. Lemor, P. Weber, M. Frenz, Combined ultrasound and optoacoustic system for real-time high-contrast vascular imaging in vivo, IEEE Trans. Med. Imag. 24 (4) (2005) 436–440.
[7] E.Z. Zhang, J.G. Laufer, R.B. Pedley, P.C. Beard, In vivo high-resolution 3D photoacoustic imaging of superficial vascular anatomy, Phys. Med. Biol. 54 (4) (2009) 1035–1046.
[8] X. Wang, Y. Pang, G. Ku, X. Xie, G. Stoica, L.V. Wang, Noninvasive laser-induced photoacoustic tomography for structural and functional in vivo imaging of the brain, Nat. Biotechnol. 21 (7) (2003) 803–806.
[9] A. de la Zerda, Y.M. Paulus, R. Teed, S. Bodapati, Y. Dollberg, B.T. Khuri-Yakub, M.S. Blumenkranz, D.M. Moshfeghi, S.S. Gambhir, Photoacoustic ocular imaging, Opt. Lett. 35 (3) (2010) 270–272.
[10] M. Xu, L.V. Wang, Time-domain reconstruction for thermoacoustic tomography in a spherical geometry, IEEE Trans. Med. Imag. 21 (7) (2002) 814–822.
[11] M. Xu, Y. Xu, L.V. Wang, Time-domain reconstruction algorithms and numerical simulations for thermoacoustic tomography in various geometries, IEEE Trans. Biomed. Eng. 50 (9) (2003) 1086–1099.
[12] Y. Xu, D. Feng, L.V. Wang, Exact frequency-domain reconstruction for thermoacoustic tomography-I: Planar geometry, IEEE Trans. Med. Imag. 21 (7) (2002) 823–828.
[13] Y. Xu, M. Xu, L.V. Wang, Exact Frequency-Domain Reconstruction for Thermoacoustic Tomography-II: Cylindrical Geometry, IEEE Trans. Med. Imag. 21 (7) (2002) 829–833.
[14] M. Xu, L.V. Wang, Pulsed-microwave-induced thermoacoustic tomography: filtered back-projection in a circular measurement configuration, Med. Phys. 29 (8) (2002) 1661–1669.
[15] M. Xu, L.V. Wang, Universal back-projection algorithm for photoacoustic computed tomography, Phys. Rev. E 71 (1) (2005). 016706-1-016706-7..
[16] C. Zhang, Y. Wang, Deconvolution reconstruction of full-view and limited-view photoacoustic tomography: a simulation study, J. Opt. Soc. Am. A 25 (10) (2008) 2436–2443.
[17] C. Zhang, C. Li, L.V. Wang, Fast and robust deconvolution-based image reconstruction for photoacoustic tomography in circular geometry experimental validation, IEEE Photonics J. 2 (1) (2010) 57–66.
[18] G. Paltauf, J.A. Viator, S.A. Prahl, S.L. Jacques, Iterative reconstruction algorithm for optoacoustic imaging, J. Opt. Soc. Am. A 112 (4) (2002) 1536–1544.
[19] C.K. Liao, M.L. Li, P.C. Li, Optoacoustic imaging with synthetic aperture focusing and coherence weighting, Opt. Lett. 29 (21) (2004) 2506–2508.
[20] D. Modgil, P.J. La Rivière, Implementation and comparison of reconstruction algorithms for 2D optoacoustic tomography using a linear array, Proc. SPIE 6856 (2008). 68561D-1.
[21] C. Li, A. Aguirre, J. Gamelin, A. Maurudis, Q. Zhu, L.V. Wang, Real-time photoacoustic tomography of cortical hemodynamics in small animals, J. Biomed. Opt. 15 (1) (2010). 010509-1-010509-3..
[22] J.K. Gamelin, A. Aguirre, Q. Zhu, Fast, limited-data photoacoustic imaging for multiplexed systems using a frequency-domain estimation technique, Med. Phys. 38 (3) (2011) 1503–1818.
[23] D.L. Donoho, Compressed sensing, IEEE Trans. Inf. Theory 52 (4) (2006) 1289–1306.
[24] J. Provost, F. Lesage, The application of compressed sensing for photo-acoustic tomography, IEEE Trans. Med. Imag. 28 (4) (2009) 585–594.
[25] Z. Guo, C. Li, L. Song, L.V. Wang, Compressed sensing in photoacoustic tomography in vivo, J. Biomed. Opt. 15 (2) (2010). 021311-1-021311-6..
[26] E. Candes, J. Romberg, T. Tao, Robust uncertainty principles: exact signal reconstruction from highly incomplete frequency information, IEEE Trans. Inf. Theory 52 (2) (2006) 489–509.
[27] L.I. Rudin, S. Osher, E. Fatemi, Nonlinear total variation based noise removal algorithms, Physica D 60 (1–4) (1992) 259–268.
[28] E.Y. Sidky, C.M. Kao, X. Pan, Accurate image reconstruction from few-views and limited-angle data indivergent-beam CT, J. X-Ray Sci. Technol. 14 (2) (2006) 119–139.
[29] S.J. LaRoque, E.Y. Sidky, X. Pan, Accurate image reconstruction from few-view and limited-angle data in diffraction tomography, J. Opt. Soc. Am. A 25 (7) (2008) 1772–1782.
[30] E.Y. Sidky, X. Pan, Image reconstruction in circular cone-beam computed tomography by constrained total variation minimization, Phys. Med. Biol. 53 (17) (2008) 4777–4807.
[31] L. Yao, H. Jiang, Photoacoustic image reconstruction from few-detector and limited-angle data, Biomed. Opt. Express 2 (9) (2011) 2649–2654.
[32] K. Wang, E.Y. Sidky, M.A. Anastasioa, A.A. Oraevsky, X. Pan, Limited data image reconstruction in optoacoustic tomography by constrained, total variation minimization, Proc. SPIE 7899 (2011). 78993U-1.
[33] R.A. Kruger, P. Liu, Y. Fang, C.R. Appledorn, Photoacoustic ultrasound (PAUS)-reconstruction tomography, Med. Phys. 22 (10) (1995) 1605–1609.